

# Locomotion of Sensor-Integrated Soft Robotic Devices Inside Sub-Millimeter Arteries with Impaired Flow Conditions

Lucio Pancaldi, Lorenzo Nosedà, Amit Dolev, Adele Fanelli, Diego Ghezzi, Andrew J. Petruska, and Mahmut Selman Sakar\*

One of the grand challenges in interventional cardiology and neuroradiology is to minimize the operation time and risk of damage during catheterization. These two factors drastically increase if the target location resides in small and tortuous vessels. Flow-driven microcatheters are capable of rapidly and safely navigating small arteries with complex anatomy. However, their navigation relies on proper perfusion, which is an important bottleneck in the treatment of pathologies that cause impaired flow conditions. This work introduces the first endovascular sensor-integrated soft robotic device that navigates sub-millimeter arteries by extracting propulsive power from external magnetic fields. To this end, a number of innovations are described in the design, actuation, and control of flexible magnetic structures. The device is capable of advancing inside vasculature in an automated fashion using an open-loop control scheme. Onboard sensors enable the real-time monitoring of flow conditions, and autonomous switching between different modes of locomotion. The potential of the presented technology for minimally invasive diagnosis and therapy is demonstrated by achieving navigation inside coronary arteries of an ex vivo porcine heart under fluoroscopic guidance.


the aid of a fluoroscope, a real-time X-ray imaging system. The guidewire serves as a guide during the placement and removal of the larger tube-shaped catheter. Steering guidewires and endovascular devices using robotic actuation promise to improve the speed, safety, and efficacy of interventions.<sup>[7–24]</sup> Integration of electronic devices on endovascular instruments such as force, temperature, pressure, and flow sensors<sup>[25–27]</sup> facilitated the development of intelligent machines that are capable of navigating the cardiovascular system autonomously.<sup>[28]</sup> Sensor-integrated catheters have been miniaturized to millimeter<sup>[29–32]</sup> and even micrometer scale<sup>[33]</sup> using microengineering methods. Despite these technological advances, catheterization of tortuous small vessels using the conventional push-based navigation technique is still tedious, time-consuming, and can damage the vasculature. As a result, a significant portion of the human vasculature remains clinically inaccessible to tethered diagnostic and therapeutic tools.

## 1. Introduction

Interventional cardiology and neuroradiology have revolutionized medicine by offering minimally invasive endovascular procedures to treat various life-threatening conditions such as stroke, arteriovenous malformations, aneurysms, atherosclerosis, and cancer.<sup>[1–6]</sup> In the majority of these procedures, the physician manually steers a guidewire to the target site with

We have recently discovered a navigation method that exploits hydrokinetic energy to transport ultraflexible microfabricated electromechanical devices without the aid of a guidewire.<sup>[34]</sup> The devices were designed to have a cross-sectional profile that drastically increased their compliance, allowing the coupling between their motion and the dynamics of the blood flow inside tortuous vessels. The ribbon shape also affords the incorporation of onboard flow sensors using conventional cleanroom

L. Pancaldi, L. Nosedà, A. Dolev, M. S. Sakar  
Institute of Mechanical Engineering and Institute of Bioengineering  
Ecole Polytechnique Fédérale de Lausanne  
1015 Lausanne, Switzerland  
E-mail: selman.sakar@epfl.ch

 The ORCID identification number(s) for the author(s) of this article can be found under <https://doi.org/10.1002/aisy.202100247>.

© 2022 The Authors. Advanced Intelligent Systems published by Wiley-VCH GmbH. This is an open access article under the terms of the Creative Commons Attribution License, which permits use, distribution and reproduction in any medium, provided the original work is properly cited.

DOI: 10.1002/aisy.202100247

A. Fanelli, D. Ghezzi  
Medtronic Chair in Neuroengineering  
Centre for Neuroprosthetics and Institute of Bioengineering  
1202 Geneva, Switzerland

A. J. Petruska  
Mechanical Engineering Department  
Colorado School of Mines  
Golden, CO 80401, USA

techniques. Homogenous magnetic fields are applied at vasculature bifurcations to tilt the magnetic head and generate lift forces, to facilitate the entry of the tip into the target lumen. The dependence on the hydrodynamic force, however, prohibits the use of this technology in situations where blood flow is impaired, namely in obstructed arteries. The obstruction could be caused by embolism, thrombosis, and traumatic injury, all of which would require endovascular monitoring and interventions.

Here, we present a wireless actuation methodology to transport ultraflexible sensor-integrated robots throughout the microvasculature without the aid of physiological flow. Recent work has shown that small pieces of magnetic elastomer sheets could be actuated using time-varying homogeneous magnetic fields to generate undulatory motion or inchworm-like gait within closed channels.<sup>[35–37]</sup> The idea of magnetically actuating and steering endovascular instruments precedes the use of guidewires, and magnetic navigation was extensively explored by the para-operation device (POD) catheters, although at much larger scales.<sup>[38–40]</sup> Inspired by these studies, we postulated that the thrust generated by an undulating magnetic head could pull an ultraflexible tether inside vessels with the impaired flow (hypoperfusion) or no flow. The soft robotic device consists of a flexible polyimide ribbon that carries onboard sensors, and a head made of a magnetorheological elastomer (**Figure 1a**). We systematically explored the geometric design and magnetization of the head as well as the waveform of the actuation signal to optimize the navigation performance.

## 2. Results and Discussion

The first prototype consists of a ribbon-shaped head with an axially symmetric harmonic magnetization profile. The device was inserted into a channel phantom such that the Roll axis was parallel to the longitudinal axis of the channel (**Figure 1b**). A rotating circular magnetic field of nominal magnitude  $B_N$  and frequency  $f$  imposes periodic spatiotemporal torques on the internal magnetic dipoles. This periodic magnetic field generates undulations of the head, which effectively pull the tether inside the saline-filled rectangular channels (**Figure 1c**).

A robust kinematic performance was achieved when the magnetic field was rotated on the plane where the Yaw and Roll axes reside—hereon referred to as the “actuation plane” (**Figure S1, Supporting Information**). It is generally accepted that undulatory motion follows the following pattern: higher actuation frequencies generate higher forward velocity provided that the magnetic field is strong enough to dictate the deformation of the head. We performed a parametric sweep of the magnetic field (from 5 mT up to 40 mT) and the actuation frequency (from 1 Hz up to 30 Hz) within the capabilities of the electromagnetic system. The highest forward velocity was recorded at  $f = 20$  Hz and  $B_N = 25$  mT (**Figure S2, Supporting Information**). The channel width,  $w$ , is also expected to play an important role in the crawling of the head. The forward velocity of the devices monotonically increased with increasing  $w$  up to a certain threshold, reaching a maximum value of  $2.46 \text{ mm s}^{-1}$ . The velocity was able to increase

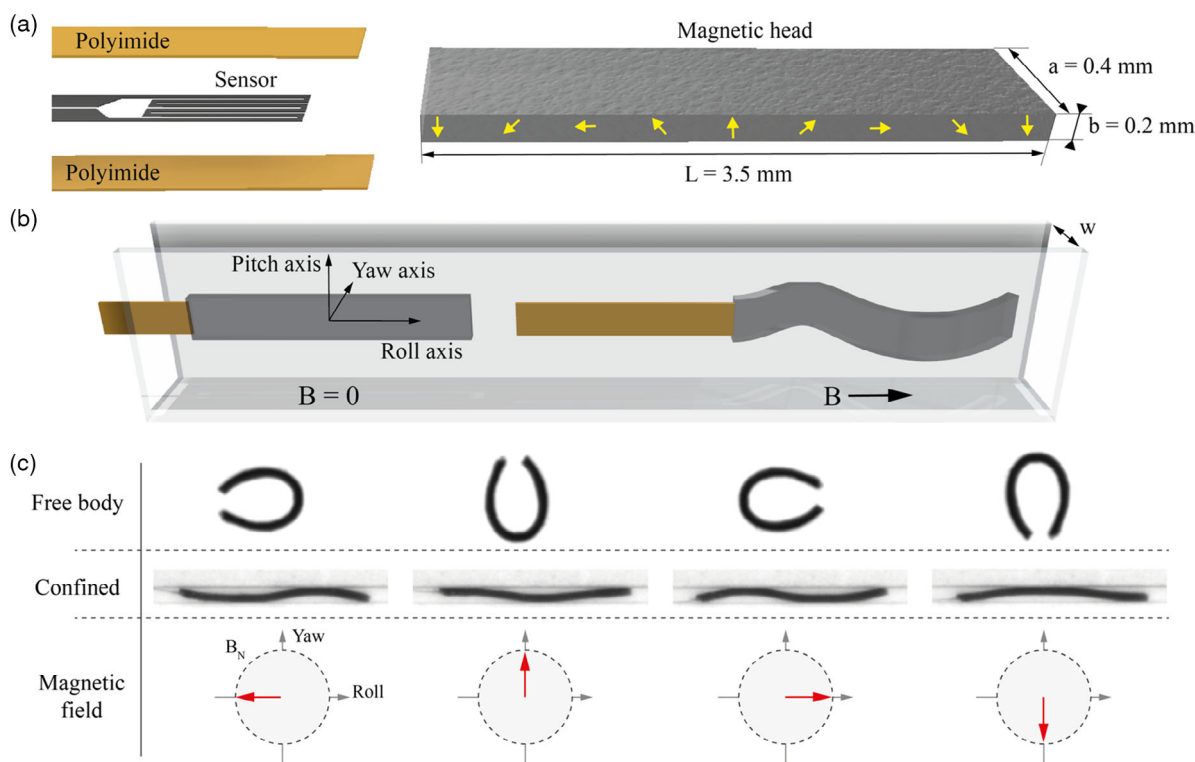


**Figure 1.** Development of the sensor-integrated soft robotic device. a) Illustration showing the individual components of the device; the polymer tether ( $250 \mu\text{m} \times 3 \mu\text{m}$  cross-section) with embedded flow sensor and the ferromagnetic head. Yellow arrows indicate the alignment of the magnetic dipoles. b) (Left) Illustration showing the roll, pitch, and yaw axes of the device inside a rectangular channel. (Right) Upon application of the actuation field,  $B_N$ , the head bends and contacts the channel walls. c) The shape of an untethered magnetic head along with the shape the same head takes when it is attached to the tether and inserted into a 0.3 mm-wide rectangular channel. The rotating uniform magnetic field is applied on the roll–yaw plane.

because the head could attain larger amplitude strokes during each actuation cycle (Figure S3, Supporting Information). Increasing  $w$  further led to a reduction in velocity because the structures struggled to contact the walls.

Blood vessels have nominally circular profiles; thus, tests performed inside rectangular channels may not be representative of cardiovascular interventions. Indeed, the device could not reliably move forward inside phantoms with a circular cross-sectional profile. Unlike rectangular channels, round channels do not restrain the device from rolling, and as a result, mechanical instabilities generated by torsion led to erratic twists (Figure 2a). Notably, the distal tip of the head twists around the roll axis, and this undesirable deformation propagates backward (Figure 2b and Movie S1, Supporting Information). As a result, the

magnetic dipoles gradually drift away from the actuation plane, which generates torsion, and ultimately disrupts the overall motion. This observation is consistent with the results of a recent article wherein untethered magnetic devices were reported to display erratic motion inside circular channels.<sup>[37]</sup> This issue could be addressed by rotating the untethered devices like a screw or rolling them like a wheel. However, these modes of locomotion are not suitable for tethered devices as a continuous rotation of the head can cause twisting or wrapping of the tether, and is mechanically limited by the construction.

We propose two complementary upgrades to avoid mechanical instabilities during actuation and generate propulsive undulations over the course of navigation. First, we postulated that the twisting of the elastic head could be constrained at the distal

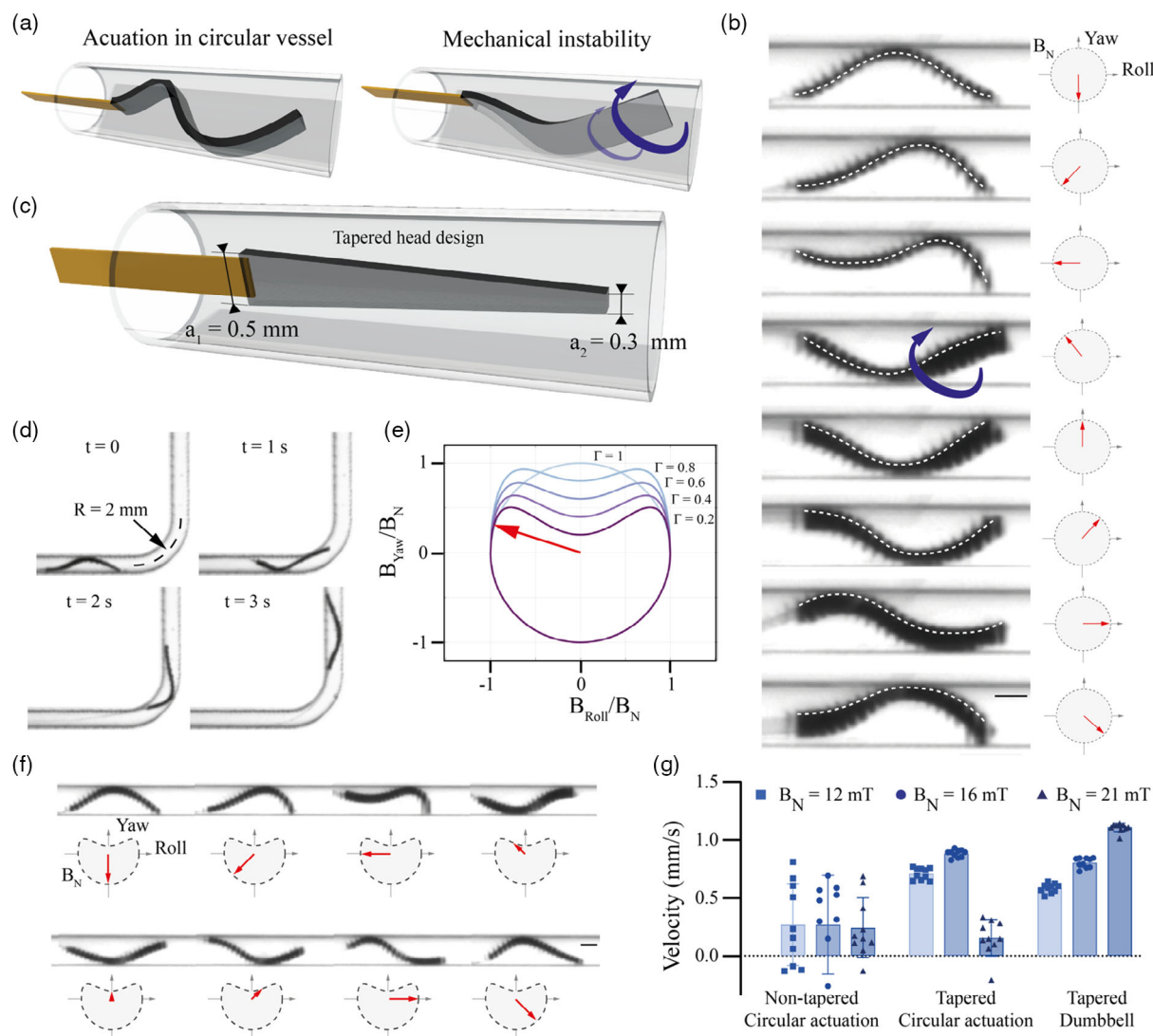


**Figure 2.** Robust crawling inside channels with a circular profile. a) A mechanical instability is generated when the magnetic head twists, which is accompanied by the loss of contact with the channel wall. b) Snapshots from the actuation of the rectangular magnetic head inside a circular channel. c) Illustration showing a width-tapered magnetic head inside a circular channel. d) Snapshots of the device crawling through a 1 mm-diameter channel with a 90°-turn. e) Shape of the dumbbell magnetic control function at different  $\Gamma$  values. f) Snapshots over an actuation cycle showing beneficiary effects of the tapered head design on the stabilization of the pose. The channel diameter is 1 mm. g) Bar plot highlighting the synergistic effects of using a tapered magnetic head and the dumbbell waveform on the forward velocity of locomotion. Scale bars, 500  $\mu\text{m}$ .

tip by decreasing the torsional rigidity at this region. The angle of twist,  $\theta$ , scales inversely with the torsional stiffness as follows.

$$\theta = \frac{TL}{GJ} \quad (1)$$

where  $G$  is the shear modulus of the material,  $J$  is the polar moment of inertia (the product  $GJ/L$  can be interpreted as the torsional stiffness),  $T$  is the applied torque, and  $L$  is the ribbon's length. For the rectangular geometry of the magnetic head, the torsional constant in Equation (1) is given by  $J = a_R b_R^3 \left[ \frac{1}{3} - 0.21 \frac{b_R}{a_R} \left( 1 - \frac{b_R^4}{12a_R^4} \right) \right]$ , where  $a_R$  and  $b_R$  denote the width and the thickness of the ribbon, respectively.<sup>[41]</sup> We designed the head as a linearly decreasing taper that confines the twist at the tip, therefore, protecting the rest of the head from the out-of-axis deformation. This intuition can be supported by modal analysis. When calculating the first normal vibration mode of ribbons, tapering the ribbon shifts the nodal point toward the distal tip (Supplementary Note 1).<sup>[42]</sup> It is also found that the relative torsion magnitude, at a given axial position, is decreased with increased taper angle.

To further clarify the role of the taper, we made a mesoscale demonstration where we rotated one end of magnetic elastomer structures by 180° while keeping the other end clamped (Figure S4, Supporting Information). While the half-torsion point was situated exactly in the middle between the two ends of the structure with a rectangular shape, repeating the same procedure with a tapered structure resulted in the appearance of the half-torsion point closer to the tapered end. Following this insight, we fabricated a magnetic head with an isosceles trapezoid shape, where the proximal base  $a_1$  is larger than the distal base  $a_2$ . The taper index is defined as  $\delta = \frac{a_2 - a_1}{a_1}$ , and we fixed this value at  $\delta = -0.4$  (Figure 2c), which we found empirically to be an optimal tradeoff between torsional-response and magnetic volume. Smaller  $\delta$  values would improve stability but also decrease the magnetic volume at the tip. We found that tapering the width of the head substantially improved the mechanical stability of the structure, and as a result, facilitated progressive navigation. We tested the maneuverability of the devices in many different channels, with 90° turns at various radii  $R$ , and found that navigation is guaranteed for  $0.5 < R < 5$  mm (Figure 2d). At radii smaller than 0.5 mm, the advancement often failed due to insufficient contact with the channel walls.

The diameter is expected to change in obstructed arteries. We tested whether the magnetic head could advance in a channel with a varying diameter. To this end, we fabricated an hour-glass-shaped glass capillary using thermal pulling. The inner diameter of the channel decreases from 0.9 to 0.6 mm in the middle of the stenotic region (Figure S5, Supporting Information). Once actuated with as field of  $B_N = 15$  mT and  $f = 5$  Hz, the device managed to navigate the whole channel. The forward velocity decreased by 60% inside the stenotic area. A constant forward velocity could be maintained by adapting the actuation signal to the channel size. We have also studied the effect of fluid viscosity on the forward velocity, as the instrument would eventually be used inside blood vessels. We performed tests in a solution of 42% glycerol in water (w/w) to mimic the viscosity of blood.<sup>[43,44]</sup> The device moved with the same forward velocity as in water at different actuation frequencies (i.e.,

up to 20 Hz), revealing that interactions between the viscous fluid and the structure were negligible in this range.

So far, we tried to resolve the negative impact of the magnetic twist by modifying the structural design of the head. A complementary solution lies in the control of the actuation signal. There exists a time period during each actuation cycle where the magnetic dipoles at the distal end of the head are aligned in the opposite direction of the actuation signal. We aimed to mitigate the torsion induced by this transient antiparallel alignment of the distal magnetic dipoles with respect to the rotating magnetic field. To this end, we modified the control signal in a way that lower torque was applied on the distal magnetic dipoles during this time period. The new magnetic waveform, which we call the dumbbell actuation signal, presents a cusp  $\Gamma$  that indents the previous circular trajectory along the yaw axis (Figure 2e). The dumbbell actuation signal is parameterized as follows.

$$\begin{aligned} B_{\text{Roll}}(t) &= B_N \left( \frac{4t-T}{T} \right), B_{\text{Yaw}}(t) = B_N \left( \left( \frac{4t-T}{T} \right)^2 + \Gamma \right) \sqrt{1 - \left( \frac{4t-T}{T} \right)^2} \\ \text{for } t &= [0, T/2] \\ B_{\text{Roll}}(t) &= B_N \cos \left( 2\pi \frac{t-T}{T} \right), B_{\text{Yaw}}(t) = -B_N \sin \left( 2\pi \frac{t-T}{T} \right) \\ \text{for } t &= [T/2, T] \end{aligned} \quad (2)$$

In Equation (2),  $\Gamma \in [0, 1]$ . When  $\Gamma = 0$ , the curve indents downwards and crosses the origin, leading to a zero-field stationary condition. When  $\Gamma = 1$ , the actuation signal is imposed circularly. Through trial and error, we recorded the best performance at  $\Gamma = 0.4$ . In the presence of the dumbbell control, the tip was less subjected to torsion, and the head appeared to be maintained at the correct pose during the whole actuation cycle (Figure 2f). A systematic characterization of the device motion at different  $f$ ,  $\Gamma$  and  $B_N$  showed the synergistic effects of the two proposed upgrades (Figure 2g). Devices with the tapered head design reached forward velocities as high as  $1.26 \text{ mm s}^{-1}$  at  $B_N = 21$  mT and  $f = 1$  Hz under the dumbbell actuation signal (Movie S2, Supporting Information). The results were repeatable over several devices and trials (Figure S6, Supporting Information). The contribution of the dumbbell actuation paradigm was obvious at higher magnetic fields, where the head lost stability under a rotating magnetic field with a circular profile. Locomotion at higher magnetic fields is not only useful to reach higher speeds, but also instrumental to cope with scenarios that require larger thrust. For example, relatively high friction forces arise from prolonged navigation in tortuous channels or moving against gravity. A 30%-increase in the magnetic field amplitude resulted in a 20% increase in velocity (Figure S7, Supporting Information). Unless specified, the following experiments were performed adopting a tapered magnetic head and an actuating dumbbell waveform ( $\delta = -0.4$  and  $\Gamma = 0.4$ ).

So far, we have demonstrated that the magnetic head can be used as a remotely controlled propulsion system to transport an ultraflexible tether through round-sectioned channels with curvilinear shapes. Next, we asked whether we could steer the devices in the presence of bifurcating channels. Control on heading was implemented by generating an offset in the Center of Rotation ( $C_{\text{Rot}}$ ) on the actuation plane, i.e.,  $C_{\text{Rot}} = (dB_{\text{Roll}}, dB_{\text{Yaw}})$  (Figure 3a). As a result, the tip of the head maintains its stable undulatory motion while leaning toward the selected daughter

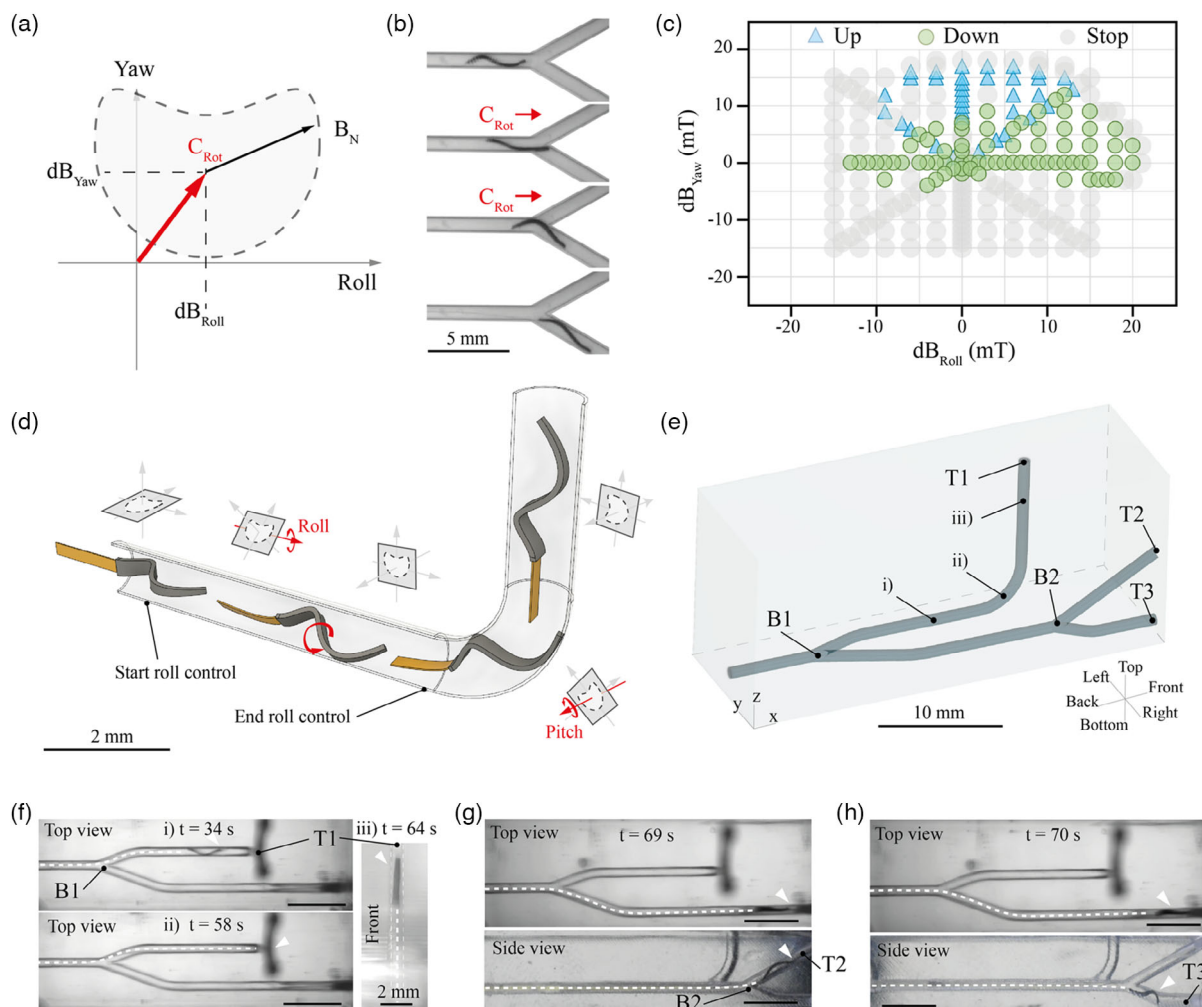


**Figure 3.** Open-loop control of automated 3D navigation. a) An offset in  $C_{Rot}$  is used to steer the device at bifurcations. b) Snapshots showing the steering of the device into the lower channel by applying an offset in  $C_{Rot}$ . c) A plot of  $C_{Rot}$  offset values leading to upward (blue triangles) and downward (green circles) motion. Gray circles correspond to impaired locomotion. The control parameters are  $B_N = 15$  mT,  $\Gamma = 0.2$ , and  $f = 1$  Hz. d) Schematic representation of the 3D steering strategy where the head is rolled before a turn that involves moving upwards or downwards. e) Schematic showing the 3D map of the phantom with two bifurcations, B1 and B2, and the three target points T1, T2, and T3. Snapshots from a successful automated navigation attempt that resulted in reaching all three target points are shown in f–h). The control parameters are  $B_N = [10\text{--}20]$  mT,  $f = 1$  Hz and  $\Gamma = 0.2$ . Scale bars, 5 mm.

vessel. As an important remark, the orientation of  $\Gamma$  must be actively maintained parallel to  $R$  at all times.

We studied the effects of the dumbbell offset control on the efficacy of crawling in a biomimetic phantom (Figure 3b and Movie S3, Supporting Information). The bifurcation consisted of two symmetric daughter channels diverting at  $30^\circ$  from the incident mother channel. Favorable  $C_{Rot}$  values for upward and downward steering are summarized in Figure 3c. The region at which we could reliably control the heading was confined to the first quadrant, and equally populated by parameters that would guide the device to the top or the bottom channel. Notably, negative  $dB_{Yaw}$  values precluded passage through the bifurcation. This restriction was due to the modified shape of the dumbbell ( $\Gamma = 0.2$ ,  $B_N = 15$  mT,  $f = 1$  Hz), which made the entire waveform fall in the lower quadrants, even at slightly

negative  $dB_{Yaw}$  values. A closer look at the kinematics revealed that the full undulatory motion was lost because the head showed a strong forward motion followed by a weak backward motion, which severely compromised the advancement (Figure S8, Supporting Information).

The bending stiffness scales cubically with the thickness, and the thickness of our devices is 10 times smaller than their width. As a result of the  $10^4$ -fold higher flexibility around the pitch axis, bending around the yaw axis is extremely unfavorable. Therefore, while navigating inside 3D curvilinear vessels, roll correction must be implemented through the magnetic torque. The idea is to put the device in a configuration so that steering at a bifurcation would require bending around the favorable Pitch axis (Figure 3d). At the entry of each turn, the yaw axis is parallel to  $R$  and the roll axis is tangential to the channel. Roll

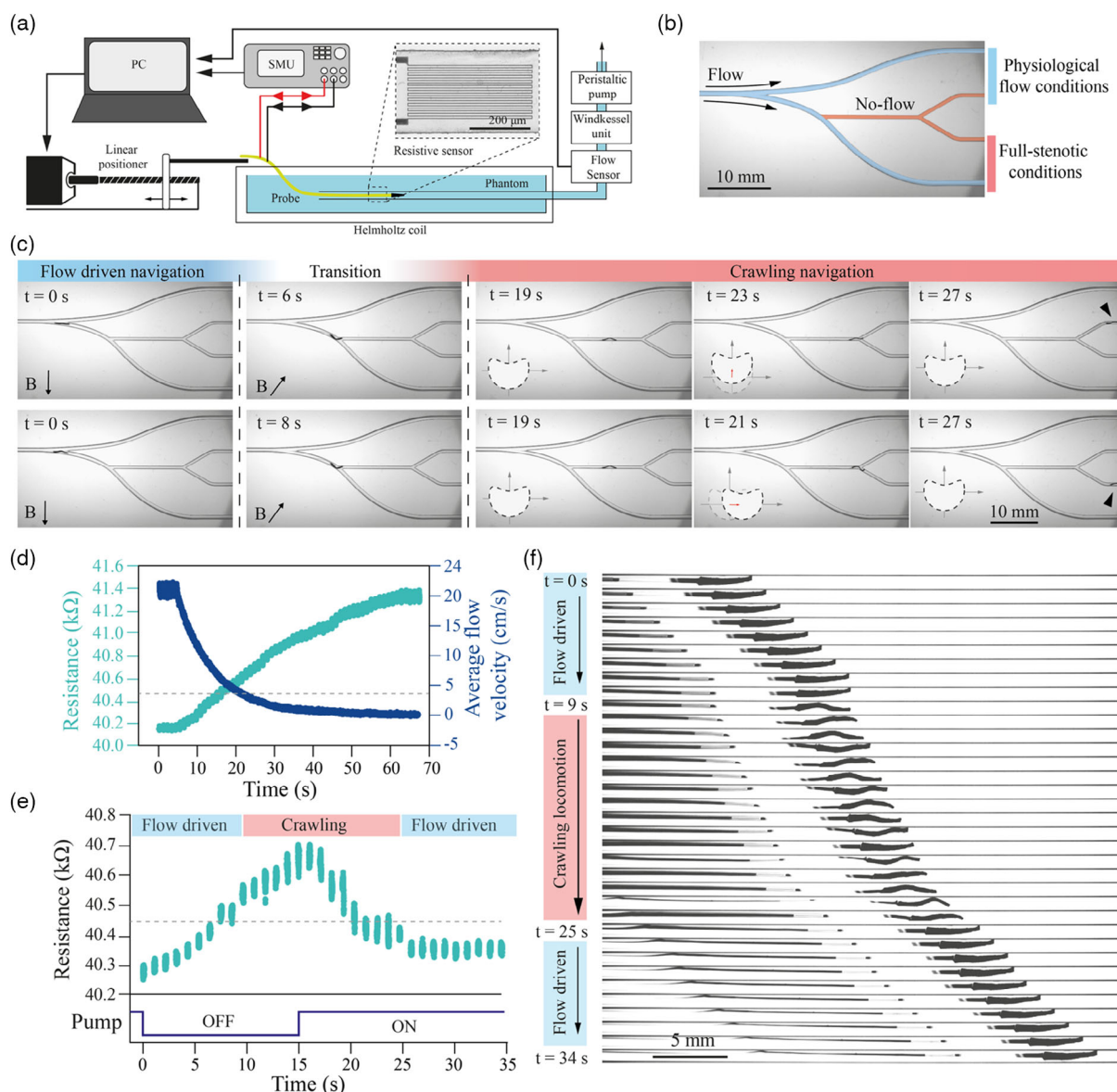


**Figure 4.** Closed-loop feedback control for multimodal locomotion. a) Experimental setup for operating the onboard sensor and setting the flow conditions inside the microfluidic channel. Inset shows a picture of the electronic sensor micro-engineered on the tether of the device. b) An image of the phantom used for demonstrating multimodal locomotion. Channels that are painted blue have physiological flow conditions, while channels that are painted red are fully obstructed, i.e., flow velocity is zero. c) Static magnetic fields are used for steering during flow-driven navigation in perfusing channels and to position the head inside the obstructed channels. Application of the rotating magnetic field instantiates crawling locomotion which realizes motion and steering in the absence of flow. d) Calibration of a hot-wire resistive sensor with respect to the average flow velocity. Gray dashed line indicates the threshold for switching locomotion modes. e) Resistance measured by the onboard sensor informs the controller about the flow conditions, and this information is used by the controller to autonomously switch between crawling and flow-driven locomotion. f) Snapshot from an experiment where the transition from flow-driven to crawling and back to flow-driven advancement is coordinated autonomously by the robot.

correction involves rotating the actuation plane around the roll axis. To be able to dynamically correct for orientation while the device is crawling, the correction must be imposed gradually and over several actuation cycles. Otherwise, the magnetic dipoles may reside outside the actuation plane, which would disrupt the undulatory motion. The device must be steered in both directions, therefore, the largest possible rotation for realignment is  $\pm 90^\circ$ .

Empowered with a robust navigation strategy, we explored the possibility of automating the procedure using an open-loop controller. We fabricated a phantom that contained two bifurcations in the  $x$ - $y$  and  $x$ - $z$  planes, with channels pointing in all three cartesian axes (Figure 3e). We used the 3D geometry of the phantom to plan a trajectory. The actuation frequency and the field amplitude were maintained the same, and the controller determined when to change the waveform of the magnetic signal for

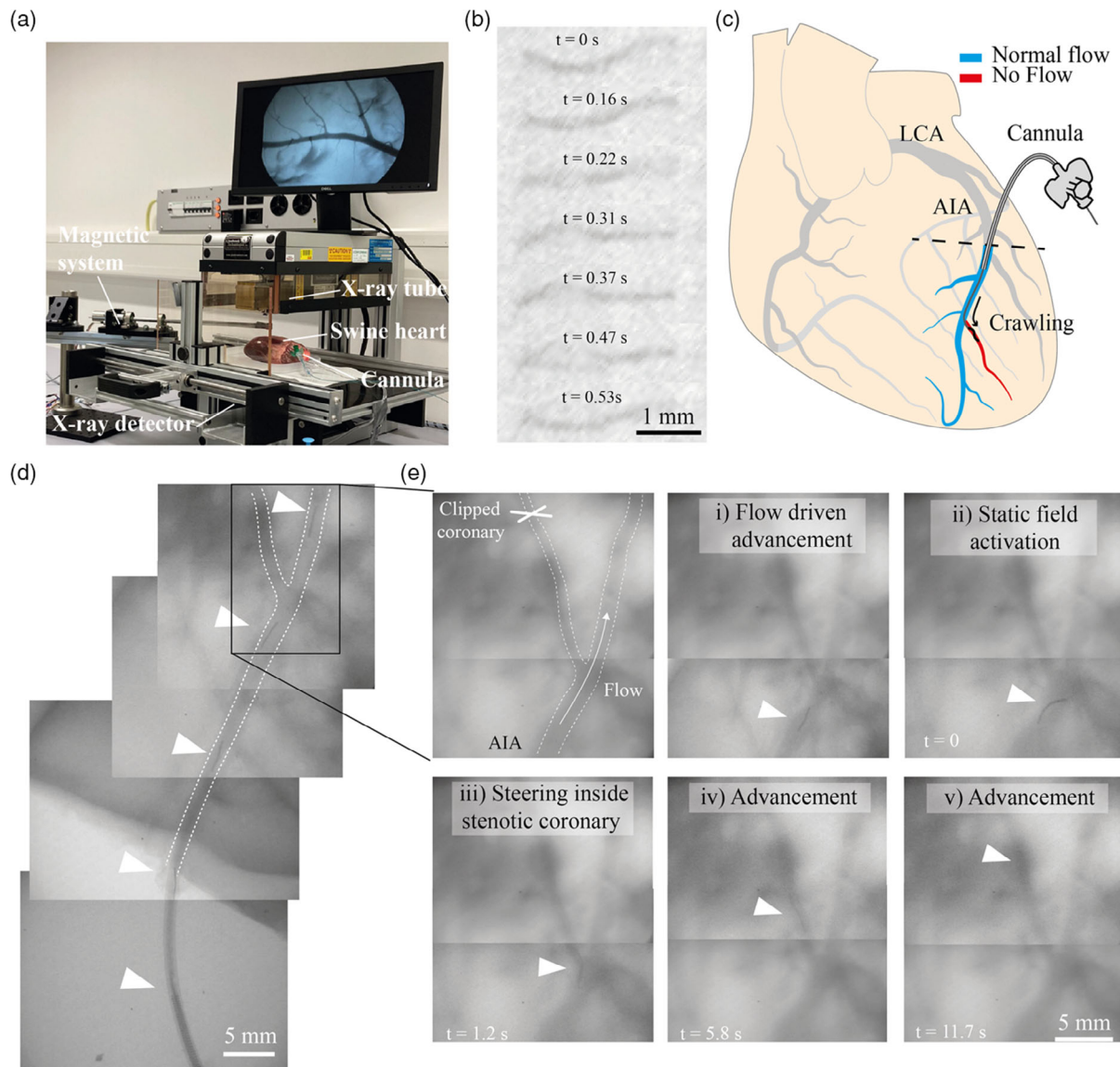


**Figure 5.** High-definition (HD)-fluoroscopy assisted multimodal navigation inside ex vivo porcine coronaries. a) Fluoroscope imaging system and the magnetic control system that consists of a rotating permanent magnet. b) X-ray images of a device crawling inside a coronary. c) Schematic representation of the porcine heart highlighting the arteries and the flow conditions. d) Flow-driven injection of the device into the coronary artery through a medical cannula. e) X-ray image showing the diverging coronary that was clipped to induce full obstruction. Application of the rotating magnetic field instantiated and navigation inside this obstructed coronary.

steering the device based on prior velocity measurements. First, the device was guided across bifurcation B1 using control parameters chosen from the plot shown in Figure 3c. After the S-shape turn, the yaw axis, which had been lying in the x-y plane (Figure 3f(i)), was gradually rotated upwards (+90° degree roll) to prepare for the vertical turn leading to target T1. During the navigation across the full length of the turn, the yaw axis was concomitantly rotated +90° around the pitch axis and maintained parallel to R all along (Figure 3f(ii)). These two maneuvers are illustrated in Figure 3d. During ascension in the vertical channel,  $f$  and  $B_N$  were increased to counteract the gravity and friction forces generated from the contact between the tether

and the channel walls (Figure 3f(iii)). After pulling back the device to the starting point, it was steered to the right daughter channel at B1. To perform the vertical bifurcation B2, the head was gradually rolled to align the yaw axis to the z-axis. Navigation across B2 into the upper (Figure 3g) and the lower (Figure 3h) channels were completed using the parameter values from Figure 3c.

We have previously shown that ultraflexible sensor-integrated soft robotic devices could be transported by the fluid flow.<sup>[34]</sup> We modified the experimental platform to incorporate the equipment required to implement flow-driven advancement including a peristaltic pump, a Windkessel unit, and flow sensors

(Figure 4a). As a first step, we verified that multimode locomotion was feasible by navigating the devices inside a microfluidic phantom with nonuniform flow conditions (Figure 4b). The navigation started with flow-driven advancement in the main channel, and the phantom contained three bifurcations along the trajectory. The main channel diverged into two daughter channels, both with physiological perfusion rate (blue channels). The device was guided to either daughter channel using static uniform magnetic fields (Figure 4c and Movie S4, Supporting Information), as described elsewhere.<sup>[34]</sup> The daughter channel with physiological flow split into two other channels where the fluid in the upper channel was completely blocked (red channels). Entry into the obstructed channel was performed by directing the head into that channel and subsequently activating the rotating uniform magnetic field. Further advancement inside the obstructed channel was accomplished with the dumbbell control, and navigation through the last bifurcation was performed by generating an offset in  $C_{\text{Rot}}$ .

Next, we investigated whether the control system could automatically switch between flow-driven advancement and crawling, depending on the flow conditions. To this end, we engineered devices with an onboard flow sensor. The flow sensor was designed in a hot wire configuration to record the change in electrical resistance upon changes in the flow conditions (Figure 4d). That is to say, a reduction in the flow rate translated into a self-heating phenomenon, increasing the resistance of the circuit. To avoid overheating, the sensor was operated in a pulsed mode at 1 Hz actuation frequency (50% duty cycle) and an acquisition rate of 1 k Hz. The device was inserted in a straight circular-profile channel, and the flow rate was modulated in such a way that the device was challenged to autonomously decide when to switch between flow-driven mode and crawling mode (Figure 4e). The light red area illustrates the temporal window in which the device activated crawling locomotion as a response to the removal of flow assistance, i.e., the average flow velocity was reduced below  $4 \text{ cm s}^{-1}$ . The sequential images in Figure 4f show an initial advancement under physiological flow followed by the autonomous activation of the crawling locomotion ( $t = 9 \text{ s}$ ). Upon reestablishment of the favorable hydrodynamic conditions ( $t = 25 \text{ s}$ ), the sensor informed the controller to switch back to the flow-driven advancement mode. To guarantee that the oscillating field does not interfere with the sensor, we compared the measurements at different actuation frequencies (Figure S9, Supporting Information) and found no statistical difference ( $P < 0.05$ ) between the groups.

The in vitro tests were done using a nested Helmholtz electromagnetic control system. However, this system was not compatible with the fluoroscope due to size constraints. To address this issue, we developed a simpler magnetic control system that consisted of a motorized rotating shaft holding a permanent magnet (Figure 5a). We first tested whether this system was capable of driving undulatory motion by actuating a magnetic head inside a glass capillary. We placed the control magnet behind the magnetic head to test whether the motion was generated due to body deformation or magnetic field gradients, and verified that the head moved away from the magnet with undulations (Movie S5, Supporting Information). Next, we confirmed that the arteries inside the ex vivo porcine heart as well as the head of our device could be visualized using the fluoroscope (Figure S10,

Supporting Information). Application of a rotating magnetic field initiated crawling motion inside a 1 mm diameter coronary artery (Figure 5b).

We aimed to repeat the in vitro multimodal locomotion paradigm inside the coronary tree of porcine ex vivo coronaries with the impaired flow (red coronary, Figure 5c). The experiment started with the perfusion of the anterior interventricular artery (AIA) branch of the left coronary artery (LCA) using a flexible cannula (Figure S11, Supporting Information). A high-concentration contrast agent was injected and maintained inside the arterial walls for at least 2 h to label all the arteries. After ejection from the cannula, the device was kept under fluidic tension and inserted inside the AIA at a perfusion rate of  $0.05 \text{ mL s}^{-1}$ . Flow-driven navigation failed in steering the device inside the obstructed artery because the distal portion was clipped with hemostat forceps, which recapitulated the hypoperfusion conditions presented by obstructed vessels (Figure 5d). We activated the control magnet to actuate the head, and the resulting undulatory motion induced by the rotating field allowed the head to crawl inside the obstructed branch (Figure 5e). To verify again that the locomotion was indeed caused by undulatory motion and was not simply due to magnetic pull, we sequentially stopped the rotation of the magnet, which repeatedly resulted in a complete cessation of motion (Figure S12, Supporting Information). Reactivation of the rotating magnetic field re-established crawling motion until reaching the distal portion of the artery.

### 3. Conclusions

Taken together, these results highlight the importance of the geometry and mechanics of the device, and the waveform of the magnetic actuation signal for locomotion in structured environments. There is no formal methodology for the design of the presented prototypes. We explored two major strategies, changing the shape of the magnetic head and applying a rotating magnetic field, primarily through intuition and trial and error. The time-varying large deflection of ferromagnetic soft continuum robots can be computed using analytical solutions and finite element modeling.<sup>[45–47]</sup> Physical interactions with the vessel wall and fluid–structure interactions may be considered in these models, as demonstrated for the modeling of soft robotic systems actuated by artificial muscles.<sup>[48]</sup> A full simulation of robot motion would reveal design and actuation parameters for optimizing the locomotion performance for any given vessel anatomy and flow conditions.

Harnessing hydrokinetic energy and contact forces open up the possibility to navigate ultraflexible robotic devices inside extreme microvasculature. Our results showed that the control performance highly depends on when and how these external factors are considered in the kinematics of the problem. In the clinical setting, the interventionalist would need to discriminate between normally perfusing and hypoperfusing vessels to choose the proper advancement mode. However, it would be challenging to measure the flow rate from fluoroscope images during operation or to make pre-operative predictions; therefore, integrating flow sensors is instrumental to implementing a multimode advancement scheme. Using onboard sensory information to assist endovascular interventions is an unconventional



strategy. The complete reliance on the capabilities of the surgeon is currently necessary partly due to the lack of instrumentation. The majority of the existing catheters and guidewires are mechanical instruments that do not carry electronic components. We microfabricated devices using manufacturing processes compatible with the engineering of flow sensors to enable real-time data acquisition. Carrying onboard flow and pressure sensors has paramount importance to perform a complete assessment of the physiological state of the cardiovascular system.<sup>[49]</sup> Fast and accurate measurement of the pressure and absolute flow within the coronary arteries, for example, is instrumental for the cardiologist to decide whether a stent must be deployed in a stenotic area. In this regard, our soft robotic devices can serve a unique function, probing the peripheral cerebrovascular arteries for the diagnosis of vascular conditions.

As a step forward, we described materials and methods that empower the robotic devices with the capability to autonomously switch between flow-driven and crawling-based motion. Solving the navigation problem for microfabricated electromechanical devices advances the robotics research field from teleoperated interventions to machine intelligence. With the incorporation of other electronics such as pressure and chemical sensors, the device could be programmed to reach regions with pathologic conditions without external supervision.

#### 4. Experimental Section

**Experimental Setup:** The electromagnetic system was designed following the instructions reported elsewhere.<sup>[50]</sup> Briefly, a 3-axis nested Helmholtz coil generated the homogeneous magnetic fields within a space of  $22 \times 53 \times 94 \text{ mm}^3$ . The three pairs of coils measured 114, 198, and 299 mm and were capable of generating a magnetic field of 85, 60, and 50 mT. The current was supplied and modulated by three sets of power supplies (S8VK 480 W, Omron, and SM 52-AR-60, Delta Elektronika) and servo controllers (Syren25 and Syren50, Dimension Engineering). An analog/digital I/O PCI Express board (Model 826 Sensoray) interfaced with the software (programmed in MATLAB, Mathworks) and the hardware. The pulsatile flow was generated by a peristaltic pump (LP-BT100-2), Drifton). Movies were recorded using a complementary metal oxide semiconductor (CMOS) camera (acA4024-29uc, Basler). The microfluidic phantoms were fabricated by Protolabs (France) from ABS material according to CAD drawings. Alternatively, microvasculature phantoms can be fabricated using a 3D printer (Ultimaker) by sacrificial negative molding in silicone with water-soluble polyvinyl-alcohol extrusion materials.<sup>[34,51]</sup> The electrical measurements were performed using a source meter (B2902A, Keysight).

**Fabrication of the Magnetic Head:** The magnetic structures were fabricated by blade casting a mixture of silicon polymer (EcoFlex 00-10) and neodymium iron boron (NdFeB) microparticles (5  $\mu\text{m}$ , Magnequench, Germany) at a 1:1 mass ratio.<sup>[37]</sup> The slurry was filled into a well formed with 200  $\mu\text{m}$ -thick spacers and cured overnight at room temperature. The structures were cut with a flat razor blade and wrapped around a glass capillary (1 mm-diameter) such that the two ends would connect, completing a full circle. The structures were then magnetized using an impulse magnetizer (Magnet-Physik). The structures were then glued to the polyimide tether using an instant glue (Loctite 401).

**Fabrication of the Flow Sensor:** The details of the fabrication process for the sensor-integrated tether were reported elsewhere.<sup>[34]</sup> Briefly, devices have been prepared by spin-coating on a 4 inch Si wafer a 4  $\mu\text{m}$  thick layer of PI (PI2610 Hitachi Chemical DuPont MicroSystems GmbH). A positive photoresist (AZ1512, 2  $\mu\text{m}$  exposed by Heidelberg Instruments MLA150, 405 nm, and 104 mJ  $\text{cm}^{-2}$  and developed by AZ 726 MIF) has been used as a mask for sputtering (Alliance Concept AC450) a 100 nm-thick layer of

gold in stripes of 250  $\mu\text{m}$  width and 9 cm length, followed by lift-off in acetone. The borders have been then laser cut (Optec MM200-USP) and detachment from the wafer has been done manually. The fabrication of the flow sensors involves the sputtering of titanium and platinum layers serving for adhesion and electrical conduction, respectively. To add the two serpentes, designated as temperature sensor and heater, another 25 nm thick layer of platinum has been sputtered over the wafer, after surface activation by argon plasma (Alliance Concept AC450). The shapes of the traces and serpentes were defined using spin-coating and removal of positive photoresists (AZ9260, 8  $\mu\text{m}$ , and AZ1512, 2  $\mu\text{m}$ ). The electrical circuits were sandwiched between PI layers.

**Ex vivo Experiments:** Swine hearts were obtained from a local farm (LaFerme Aebischer, 1595 Faoug, Switzerland). The AIA was perfused using a flexible cannula (18 G Vasofix, B. Braun) and an intravenous (IV) bag. X-ray imaging was performed using a benchtop fluoroscope (Labscope, Glenbrook technologies) and a radiopaque contrast agent (Iopamiro 370, Bracco, Switzerland). After mapping the coronary tree, the diverging artery was clipped with hemostat forceps to recapitulate vessel obstruction. The magnetic system was composed of a 1  $\text{cm}^3$  NdFeB magnet assembled at the tip of a rotating shaft. The shaft was rotated by a DC motor (EC-i30, Maxon motor) and controlled by a servo driver (ESCON 36/3 EC, Maxon motor).

#### Supporting Information

Supporting Information is available from the Wiley Online Library or from the author.

#### Acknowledgements

This work was supported by the European Research Council (ERC) under the European Union's Horizon 2020 research and innovation program (Grant agreement No. 714609). The authors thank Dr. Dong Yan for the help with the magnetizer and Dr. Pascal Mosimann for the fruitful discussions.

#### Conflicts of Interest

The authors declare no conflict of interest.

#### Data Availability Statement

The data that support the findings of this study are available from the corresponding author upon reasonable request.

#### Keywords

endovascular interventions, magnetism, medical imaging, medical robotics, microengineering, solid mechanics

Received: December 1, 2021

Revised: February 14, 2022

Published online:

[1] Y. Zhu, H. Zhang, Y. Zhang, H. Wu, L. Wei, G. Zhou, Y. Zhang, L. Deng, Y. Cheng, M. Li, H. A. Santos, W. Cui, *Adv. Mater.* **2019**, 31, 1805452.

[2] J. T. DeVries, C. J. White, M. C. Cunningham, S. R. Ramee, *Catheterization Cardiovasc. Interventions* **2008**, 72, 705.

- [3] R. W. Crowley, A. F. Ducruet, C. G. McDougall, F. C. Albuquerque, *Neurosurgery* **2014**, *74*, S74.
- [4] B. Lubicz, L. Collignon, G. Raphaeli, J.-P. Pruvo, M. Bruneau, O. De Witte, X. Leclerc, *Stroke* **2010**, *41*, 2247.
- [5] D. R. Holmes Jr, D. Williams, *Circ. Cardiovasc. Interventions* **2008**, *1*, 60.
- [6] R. S. D'Amico, D. Khatri, N. Reichman, N. V. Patel, T. Wong, S. R. Fralin, M. Li, J. A. Ellis, R. Ortiz, D. J. Langer, J. A. Boockvar, *J. Neurooncol.* **2020**, *147*, 261.
- [7] H. Rafii-Tari, C. J. Payne, G.-Z. Yang, *Ann. Biomed. Eng.* **2014**, *42*, 697.
- [8] J. Burgner-Kahrs, D. C. Rucker, H. Choset, *IEEE Trans. Rob.* **2015**, *31*, 1261.
- [9] Y. Kim, G. A. Parada, S. Liu, X. Zhao, *Sci. Rob.* **2019**, *4*, eaax7329.
- [10] C. Chautems, A. Tonazzini, Q. Boehler, S. H. Jeong, D. Floreano, B. J. Nelson, *Adv. Intell. Syst.* **2019**, *2*, 1900086.
- [11] M. Mattmann, C. De Marco, F. Briatico, S. Tagliabue, A. Colusso, X. Z. Chen, J. Lussi, C. Chautems, S. Pané, B. Nelson, *Adv. Sci.* **2021**, *9*, 2103277.
- [12] S. Jeon, A. K. Hoshier, K. Kim, S. Lee, E. Kim, S. Lee, J. Kim, B. J. Nelson, H. Cha, B. Yi, H. Choi, *Soft Rob.* **2019**, *6*, 54.
- [13] A. Azizi, C. C. Tremblay, K. Gagné, S. Martel, *Sci. Rob.* **2019**, *4*, eaax7342.
- [14] T. Krings, J. Finney, P. Niggemann, P. Reinacher, N. Lück, A. Drexler, J. Lovell, A. Meyer, R. Sehra, P. Schauerte, M. Reinges, F. J. Hans, A. Thron, *Neuroradiology* **2006**, *48*, 394.
- [15] J. Edelmann, A. J. Petruska, B. J. Nelson, *J. Med. Rob. Res.* **2017**, *3*, 1850002.
- [16] L. B. Kratchman, T. L. Bruns, J. J. Abbott, R. J. Webster, *IEEE Trans. Rob.* **2017**, *33*, 227.
- [17] S. Gunduz, H. Albadawi, R. Oklu, *Adv. Intell. Syst.* **2021**, *3*, 2000181.
- [18] P. E. Dupont, J. Lock, B. Itkowitz, E. Butler, *IEEE Trans. Rob.* **2010**, *26*, 209.
- [19] C. Heunis, J. Sikorski, S. Misra, *IEEE Rob. Autom. Mag.* **2018**, *25*, 71.
- [20] J. J. Abbott, E. Diller, A. J. Petruska, *Annu. Rev. Control Rob. Autom. Syst.* **2019**, *3*, 57.
- [21] X. Yin, S. Guo, H. Hirata, H. Ishihara, *J. Intell. Mater. Syst. Struct.* **2014**, *27*, 3.
- [22] Y. Fu, H. Liu, W. Huang, S. Wang, Z. Liang, *Int. J. Med. Robot.* **2009**, *5*, 381.
- [23] P. Kanagaratnam, M. Koa—Wing, D. T. Wallace, A. S. Goldenberg, N. S. Peters, D. W. Davies, *J. Interventional Cardiac Electrophysiol.* **2008**, *21*, 19.
- [24] T. Gopesh, J. H. Wen, D. Santiago-Dieppa, B. Yan, J. S. Pannell, A. Khalessi, A. Norbash, J. Friend, *Sci. Rob.* **2021**, *6*, eabf0601.
- [25] D. H. Kim, N. S. Lu, R. Ghaffari, Y. S. Kim, S. P. Lee, L. Z. Xu, J. A. Wu, R. H. Kim, J. Z. Song, Z. J. Liu, J. Vimenti, B. de Graff, B. Elolampi, M. Mansour, M. J. Slepian, S. Hwang, J. D. Moss, S. M. Won, Y. G. Huang, B. Litt, J. A. Rogers, *Nat. Mater.* **2011**, *10*, 316.
- [26] D. H. Kim, R. Ghaffari, N. Lu, S. Wang, S. P. Lee, H. Keum, R. D'Angelo, L. Klinker, Y. Su, C. Lu, Y. S. Kim, A. Ameen, Y. Li, Y. Zhang, B. Graff, Y. Y. Hsu, Z. Liu, J. Ruskin, L. Xu, C. Lu, F. G. Omenetto, Y. Huang, M. Mansour, M. J. Slepian, J. A. Rogers, *Proc. Natl. Acad. Sci. USA* **2012**, *109*, 19910.
- [27] M. Han, L. Chen, K. Aras, C. Liang, X. Chen, H. Zhao, K. Li, N. R. Faye, B. Sun, J. H. Kim, W. Bai, Q. Yang, Y. Ma, W. Lu, E. Song, J. M. Baek, Y. Lee, C. Liu, J. B. Model, G. Yang, R. Ghaffari, Y. Huang, I. R. Efimov, J. A. Rogers, *Nat. Biomed. Eng.* **2020**, *4*, 997.
- [28] G. Fagogenis, M. Mencattelli, Z. Machaidze, B. Rosa, K. Price, F. Wu, V. Weixler, M. Saeed, J. Mayer, P. Dupont, *Sci. Rob.* **2019**, *4*, eaaw1977.
- [29] C. Li, C. H. Ahn, L. A. Shutter, R. K. Narayan, *Biosens. Bioelectron.* **2009**, *25*, 173.
- [30] C. Li, P. M. Wu, J. A. Hartings, Z. Wu, C. H. Ahn, D. Ledoux, L. A. Shutter, R. K. Narayan, *Appl. Phys. Lett.* **2011**, *99*, 233705.
- [31] G. Chatzipirpiridis, S. Gervasoni, F. Berlinger, S. Blaz, O. Ergeneman, S. Pane, B. J. Nelson, *Technical Digest the 18th Int. Conf. on Solid-State Sensors and Actuators Anchorage, Alaska* **2015**, pp. 1727–1730.
- [32] C. Moonla, K. Y. Goud, H. Teymourian, T. Tangkuaram, J. Ingrande, P. Suresh, J. Wang, *Talanta* **2020**, *218*, 121205.
- [33] B. Rivkin, C. Becker, B. Singh, A. Aziz, F. Akbar, A. Egunov, D. D. Karnaushenko, R. Naumann, R. Schafer, M. Medina-Sanchez, D. Karnaushenko, O. G. Schmidt, *Sci. Adv.* **2021**, *7*, eabl5408.
- [34] L. Pancaldi, P. Dirix, A. Fanelli, A. M. Lima, N. Stergiopoulos, P. J. Mosimann, D. Ghezzi, M. S. Sakar, *Nat. Commun.* **2020**, *11*, 6356.
- [35] W. Hu, G. Z. Lum, M. Mastrangeli, M. Sitti, *Nature* **2018**, *554*, 81.
- [36] L. N. Pham, J. A. Steiner, K. K. Leang, J. J. Abbott, *IEEE Trans. Med. Rob. Bionics* **2020**, *2*, 598.
- [37] Z. Ren, R. Zhang, R. H. Soon, Z. Liu, W. Hu, P. R. Onck, M. Sitti, *Sci. Adv.* **2021**, *7*, eabh2022.
- [38] E. H. Frei, J. Driller, H. N. Neufeld, I. Barr, L. Bleiden, H. N. Askenazy, *Med. Res. Eng.* **1966**, *5*, 11.
- [39] J. Molcho, H. Z. Karny, E. H. Frei, H. M. Askenasy, *IEEE Trans. Biomed. Eng.* **1970**, *2*, 134.
- [40] S. K. Hilai, W. J. Michelsen, J. Driller, E. Leonard, *Radiology* **1974**, *113*, 529.
- [41] R. J. Roark, W. C. Young, *Roark's Formulas For Stress and Strain*, 6th Ed., McGraw-Hill, New York, NY, **1989**.
- [42] J. Thomas, Ph.D. Thesis, University of Surrey, Guildford, UK, **1968**.
- [43] N. S. Cheng, *Ind. Eng. Chem. Res.* **2008**, *47*, 3285.
- [44] A. Volk, C. J. Kähler, *Exp. Fluids* **2018**, *59*, 75.
- [45] L. Wang, Y. Kim, C. F. Guo, X. Zhao, *J. Mech. Phys. Solids* **2020**, *142*, 104045.
- [46] R. Zhao, Y. Kim, S. A. Chester, P. Sharma, X. Zhao, *J. Mech. Phys. Solids* **2019**, *124*, 244.
- [47] D. Yan, M. Pezzulla, L. Cruveiller, A. Abbasi, P. M. Reis, *Nat. Commun.* **2021**, *12*, 2831.
- [48] X. Zhang, F. K. Chan, T. Parthasarathy, M. Gazzola, *Nat. Commun.* **2019**, *10*, 1.
- [49] P. A. Tonino, B. De Bruyne, N. H. Pijls, U. Siebert, F. Ikeno, M. van't Veer, V. Klauss, G. Manoharan, T. Engström, K. Oldroyd, P. N. Ver Lee, P. A. MacCarthy, W. F. Fearon, *N. Engl. J. Med.* **2009**, *360*, 213.
- [50] J. Abbott, *Rev. Sci. Instrum.* **2015**, *86*, 10.
- [51] O. Poupart, R. Conti, A. Schmocker, L. Pancaldi, C. Moser, K. M. Nuss, M. S. Sakar, T. Dobrocky, H. Grutzmacher, P. J. Mosimann, D. P. Pioletti, *Front. Bioeng. Biotechnol.* **2021**, *8*, 619858.